# Electrically reconfigurable phase-change transmissive metasurface

Cosmin Constantin Popescu<sup>1\*</sup>, Kiumars Aryana<sup>2,\*,‡</sup>, Parth Garud<sup>2</sup>, Khoi Phuong Dao<sup>1</sup>, Steven Vitale<sup>3</sup>, Vladimir Liberman<sup>3</sup>, Hyung-Bin Bae<sup>4</sup>, Tae-Woo Lee<sup>4</sup>, Myungkoo Kang<sup>5</sup>, Kathleen A. Richardson<sup>5</sup>, Matthew Julian<sup>6</sup>, Carlos A. Ríos Ocampo<sup>7</sup>, Yifei Zhang<sup>1</sup>, Tian Gu<sup>1,7</sup>, Juejun Hu<sup>1,8</sup>, and Hyun Jung Kim<sup>2,†</sup>

# **ABSTRACT**

Programmable and reconfigurable optics hold significant potential for transforming a broad spectrum of applications, spanning space explorations to biomedical imaging, gas sensing, and optical cloaking. The ability to adjust the optical properties of components like filters, lenses, and beam steering devices could result in dramatic reductions in size, weight, and power consumption in future optoelectronic devices. Among the potential candidates for reconfigurable optics, chalcogenide-based phase change materials (PCMs) offer great promise due to their non-volatile and analogue switching characteristics. Although PCM have found widespread use in electronic data storage, these memory devices are deeply sub-micron-sized. To incorporate phase change materials into free-space optical components, it is essential to scale them up to beyond several hundreds of microns while maintaining reliable switching characteristics. This study demonstrated a non-mechanical, non-volatile transmissive filter based on low-loss PCMs with a 200  $\mu$ m×200  $\mu$ m switching area. The device/metafilter can be consistently switched between low- and high-transmission states using electrical pulses with a switching contrast ratio of 5.5 dB. The device was reversibly switched for 1250 cycles before accelerated degradation took place. The work represents an important step toward realizing free-space reconfigurable optics based on PCMs.

Keywords. phase change materials; metasurfaces; photonic devices; reconfigurable optics

### 1 Introduction

Unlike traditional optics whose properties are fixed after fabrication, reconfigurable optics enable agile tuning of their functions to dynamically adapt to different needs. The applications for reconfigurable optics span adaptive optical microscopy to data communications<sup>1</sup> and observation of celestial bodies in space telescopes<sup>2,3</sup>. Thus far, various techniques have been adopted for real-time manipulation of electromagnetic wave properties (amplitude, phase, and polarization)<sup>4</sup> either for focusing, filtering or steering light such as liquid crystals<sup>5</sup>, deformable mirrors<sup>6</sup>, filter wheels<sup>7</sup>, and digital mirror devices<sup>8</sup>. While each of these methods provides advantages within their specific applications, there remains a pressing demand for a compact, non-mechanical, non-volatile beam-shaping technology capable of continuously tuning light properties. Such a technology should also be compatible with standard microfabrication processes to enable its rapid and cost-effective integration with other technologies<sup>9,10</sup>.

Active metasurfaces have emerged as a new avenue for creating compact, high-performance reconfigurable optical devices that can be electrically controlled without the need for mechanical components<sup>11–20</sup>. This innovative method for controlling

<sup>&</sup>lt;sup>1</sup>Department of Materials Science and Engineering, Massachusetts Institute of Technology, Cambridge, 02139, MA, USA

<sup>&</sup>lt;sup>2</sup>NASA Langley Research Center, Hampton, 23666, VA, USA

<sup>&</sup>lt;sup>3</sup>Lincoln Laboratory, Massachusetts Institute of Technology, Lexington, MA, 02421, USA,

<sup>&</sup>lt;sup>4</sup>KAIST Analysis Center, Korea Advanced Institute of Science and Technology, Yuseong-gu, Daejeon 34141, Korea

<sup>&</sup>lt;sup>5</sup>CREOL, The College of Optics & Photonics University of Central Florida Orlando, FL, 32816, USA

<sup>&</sup>lt;sup>6</sup>Booz Allen Hamilton Inc., Arlington, VA, 22202, USA

<sup>&</sup>lt;sup>7</sup>University of Maryland, Department of Materials Science & Engineering, College Park, MD, USA

<sup>&</sup>lt;sup>8</sup>Materials Research Laboratory, Massachusetts Institute of Technology, Cambridge, 02139, MA, USA

<sup>\*</sup>These authors contributed equally to this work.

<sup>&</sup>lt;sup>‡</sup>kiumars.aryana@nasa.gov

<sup>&</sup>lt;sup>†</sup>hyunjung.kim@nasa.gov

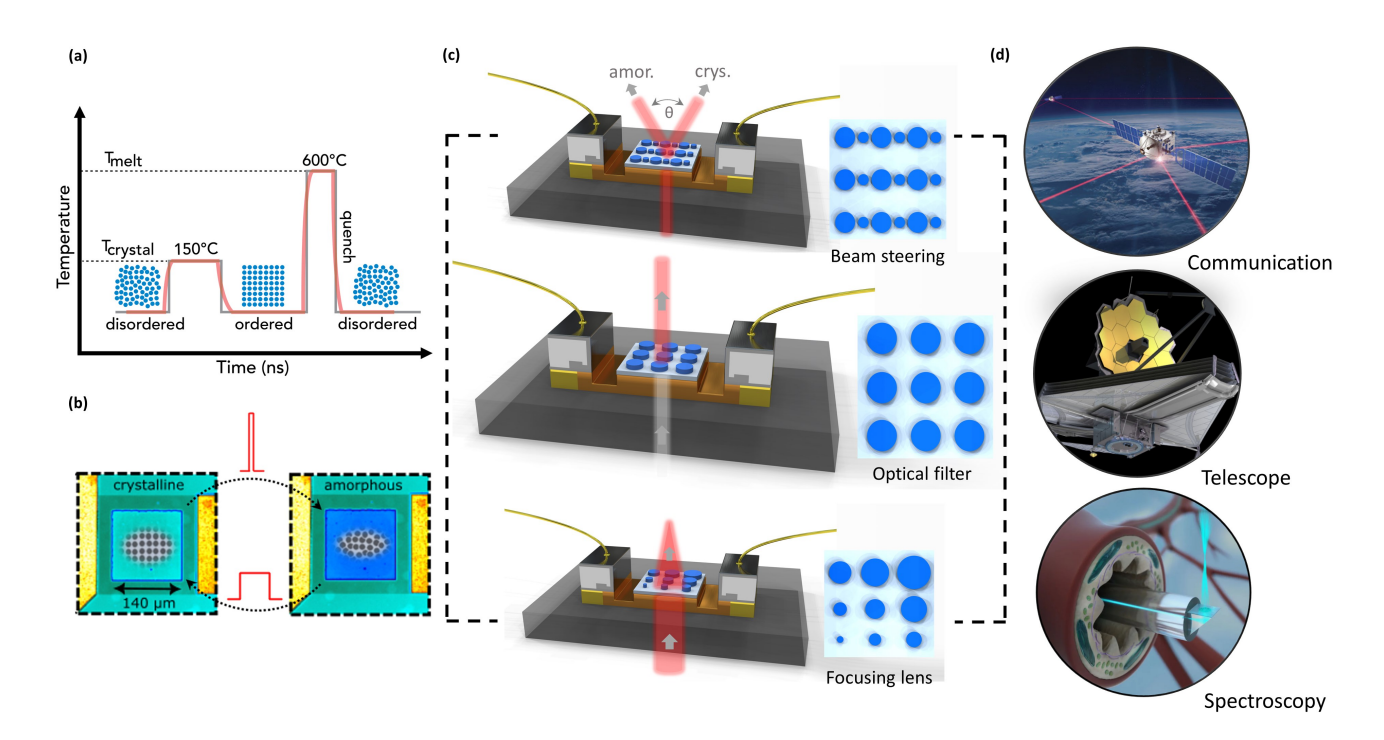


**Figure 1.** Concept of the operation of a PCM-based device, showing the temperature of the device vs. time (a) along with NIR reflection images of a PCM film after amorphization on a doped SI heater (b), types of beam manipulations highlighting the types of meta-atoms required as a minimal basis for the individual operation (c) and potential areas of application for each individual type of beam manipulation (d).

photon propagation within a highly compact configuration has led to the development of small form factor optical components that were previously only achievable through sophisticated, bulky optical systems<sup>21</sup>. By incorporating an active material, such as a chalcogenide-based phase change alloy, into these metasurfaces architecture, a large degree of tunability can be achieved through reversible phase transformation in comparison to phenomena such as the thermo-optic or electro-optic effect<sup>22–26</sup>. Initiating a phase transformation in PCMs necessitates the application of a strong thermal excitation to rapidly heat the PCM and raise its temperature above the crystallization or melting point as depicted in Fig. 1(a). In the case of electrothermal switching<sup>23,27</sup>, the thermal excitation is applied through an on-chip resistive micro-heater, yielding a form factor suited for compact chip-scale integration<sup>28–30</sup>. For instance, an almost 400% reflectance change upon phase transformation was demonstrated in a PCM metasurface integrated on a metal micro-heater<sup>11</sup>. In another work, a remarkable 11-fold change in surface reflectance was achieved in a plasmonic metasurface similarly fabricated on metal micro-heaters<sup>12</sup>. These structures hold the promise for reconfigurable devices that can manipulate the direction of propagation of the signal, tune its amplitude, and focus or defocus it (Fig. 1 (c)), capabilities needed in data processing, image acquisition and analysis. Reliable, compact, tunable non-volatile optics can aid applications with stringent requirements for size, weight, and power such as space exploration, or communication (Fig. 1(d)).

The reconfigurable metasurfaces introduced thus far are limited to operating in the reflective mode due to the use of opaque metal heaters. Optically transparent heaters in 2D arrays are crucial for facilitating the advancement of next-generation active PCM metasurface devices, suitable for transmissive optics. These optics eliminate the need for beam redirection and can easily integrate into the beam path without altering its trajectory. Doped crystalline Si features low loss in the infrared beyond its band gap and CMOS compatibility, and thus qualifies as an ideal material for transparent heaters enabling transmissive reconfigurable optics. Doped Si heaters have been employed to realize an array of waveguide-based PCM devices<sup>28,29,31–34</sup> and recently a spatial light modulator prototype<sup>35</sup>. Moreover, the endurance (lifetime) of the PCM-based devices has been limited to approximately 50 cycles in the reported literature<sup>11,35</sup>. In this work, we unveil the potential of an on-chip PCM-based metasurface that can reversibly change the optical transmissive behavior using an IR transparent silicon-on-insulator (SOI) microheater. This advancement opens the door to a variety of applications, such as compact, non-volatile, and non-mechanical tunable filters<sup>36</sup> as is the focus of this study. Our experiments successfully demonstrate reversible switching of a non-mechanical optical filter using electrical pulses for almost 1250 cycles over an effective switching area of 120µm × 120µm. This has

been achieved via a reversed architecture of the metasurface, with a fishnet region of the PCM, and increased protective layer thickness. To the best of our knowledge, this marks the first demonstration of a large-area PCM-based metasurface with reliable switching across more than 1000 switching cycles. In addition, through a detailed device characterization, we identify the key factor that contributes to device failure and propose potential solutions to extend the metafilter operational lifetime beyond thousands of cycles.

# 2 Methods

## 2.1 Computational methods

The electromagnetic simulations were performed using the rigorous coupled wave analysis (RCWA) MATLAB® library RETICOLO V8<sup>37</sup>. The refractive indices of  $Ge_2Sb_2Se_4Te$  (GSST) for intermediate crystallization states were interpolated based on the Maxwell-Garnett effective medium approximation<sup>38</sup> with the amorphous state as the host material and the crystalline phase as the inclusion using previously measured refractive indices of the two phases<sup>39</sup>. The simulations were performed from 0 to 16° incident angles in steps of 4° for both TE and TM-polarizations and averaged over the simulated incident angles and TE and TM polarizations. The field profile was simulated by assuming propagation from the silicon substrate into the meta-structure and the resulting values were multiplied by the transmittance from air into silicon averaged over wavelength, angle and polarizations. The thicknesses assumed in the simulations were as follows: silicon substrate, 1.01  $\mu$ m buried oxide (BOX), 157 nm of doped silicon, 370 nm GSST, 310 nm SiN<sub>x</sub>, and air. Metafilters with various periods and hole sizes were fabricated for testing. For the Fourier transform infrared (FTIR) data collection and simulation, the dimensions were estimated as 445 nm × 445 nm size hole with 700 nm period. According to scanning electron microscopy (SEM) observation, a 60 nm layer of SiN<sub>x</sub> was coated on the bottom of the hole and on the walls of GSST resulting from the incomplete covering of the walls and the incomplete filling of the structure due to nonconformal sputtering deposition.

#### 2.2 Fabrication Methods

The major steps in the fabrication process of the metasurface devices are illustrated in Fig. 2. Details of the SOI micro-heater fabrication were elaborated elsewhere<sup>34,40</sup>. The thickness of the buried oxide used was 1.01  $\mu$ m and the doped Si layer thickness was 157 nm with around 5 × 10<sup>20</sup> cm<sup>-3</sup> maximum doping concentration from 80 keV phosphorous ion-implantation. The inclusion of buried oxide may result in substantial absorption in the mid to far IR range, which is undesirable. For applications within this spectrum, replacing the buried oxide layer with a buried nitride layer<sup>41,42</sup>, or considering a silicon-on-sapphire-based heater, given that transient thermal requirements can be met, could offer a wider operational range.

Large squares for the initial blanket GSST deposition are defined in AZ nLOF 2020 using an MLA 150 Heidelberg at 375 nm. The prebaking and post-exposure baking were done at a nominal 112 °C for 60 s on a hot plate. An optimal dose was observed around or slightly above 155 mJ/cm<sup>2</sup>. The development was done in AZ 300 MIF for around 70-80 s. Thin films of GSST of 370 nm thickness were deposited via thermal evaporation at a base pressure of  $1.8 \times 10^{-6}$  Torr onto the chip. 10 nm of SiO<sub>2</sub> were evaporated via e-beam evaporation before resist removal for protection against oxidation. The resist was removed via overnight soaking in n-methylpyrrolidone (NMP), followed by acetone and isopropanol (IPA) rinse. 50 nm of polymethyl methacrylate (PMMA) 495 K followed by 350 nm of ZEP 520 A e-beam resist were spin coated and pre-baked sequentially at 180 °C on a hot plate. The PMMA layer served the purpose of aiding resist removal after reactive ion etching (RIE). The metasurface mask was exposed at 50 kV using a current of 10 nA in an Elionix-HS50 with proximity effect correction at a dose of 170 μC/cm<sup>2</sup>. The resist was developed in IPA: methyl isobutyl ketone (MIBK) 3:1 for 90 s and rinsed with IPA for 20 s. The resist was allowed to dry in air to prevent mechanical damage to the metasurface mask. The PCM was etched via RIE with CF<sub>4</sub>:Ar (43:15 standard cubic centimeter per minute, sccm) at 0.5 Pa, 100 W bias power and 50 W inductively coupled plasma (ICP) power in a Samco-RIE 230iP for 230 s. The electron beam resist was then removed in NMP overnight, followed by the acetone and IPA rinse. Subsequently, the PCM metasurface was encapsulated with 20 nm of Al<sub>2</sub>O<sub>3</sub> deposited at 150 °C in a Cambridge Nanotech Savannah 200. A further protective layer of SiNx was deposited via reactive sputtering from a Si target and a Si<sub>3</sub>N<sub>4</sub> target in N<sub>2</sub>: Ar atmosphere at 3 mTorr with 6:6 sccm flow rates using an AJA ATC Orion 5 chamber. The thickness of the deposited nitride was 310 nm. The region above the aluminum contacts was patterned and etched via RIE with a mixture of SF<sub>6</sub>:Ar 6:20 sccm standard recipe. A 10 μm buffer region from the edge of the metal contacts was left unetched to prevent shorting in the subsequent steps of defining an aperture. Aluminum apertures are thermally evaporated around the heaters to limit the transmitted light just to the region with metasurfaces at a base pressure of around  $9 \times 10^{-6}$  Torr. To protect the structures during backside polishing, 5 µm of PMMA 950 A were spin coated onto the substrate. The sample backside was then mechanically polished to enable transmissive measurements with minimal roughness scattering. The sample was secured to a support structure with CrystalBond™ wax before mechanical polishing with sequentially smaller particle size lapping paper (SiC 15  $\mu$ m, 5  $\mu$ m, 3  $\mu$ m and Al<sub>2</sub>O<sub>3</sub> 1  $\mu$ m). The samples were removed from the support structure and rinsed in acetone and IPA to remove the wax and protective PMMA resist (2 (b,c)). Finally, the samples were mounted onto a custom-designed printed circuit board and wire bonded with a ball bonder MEI 1204D.

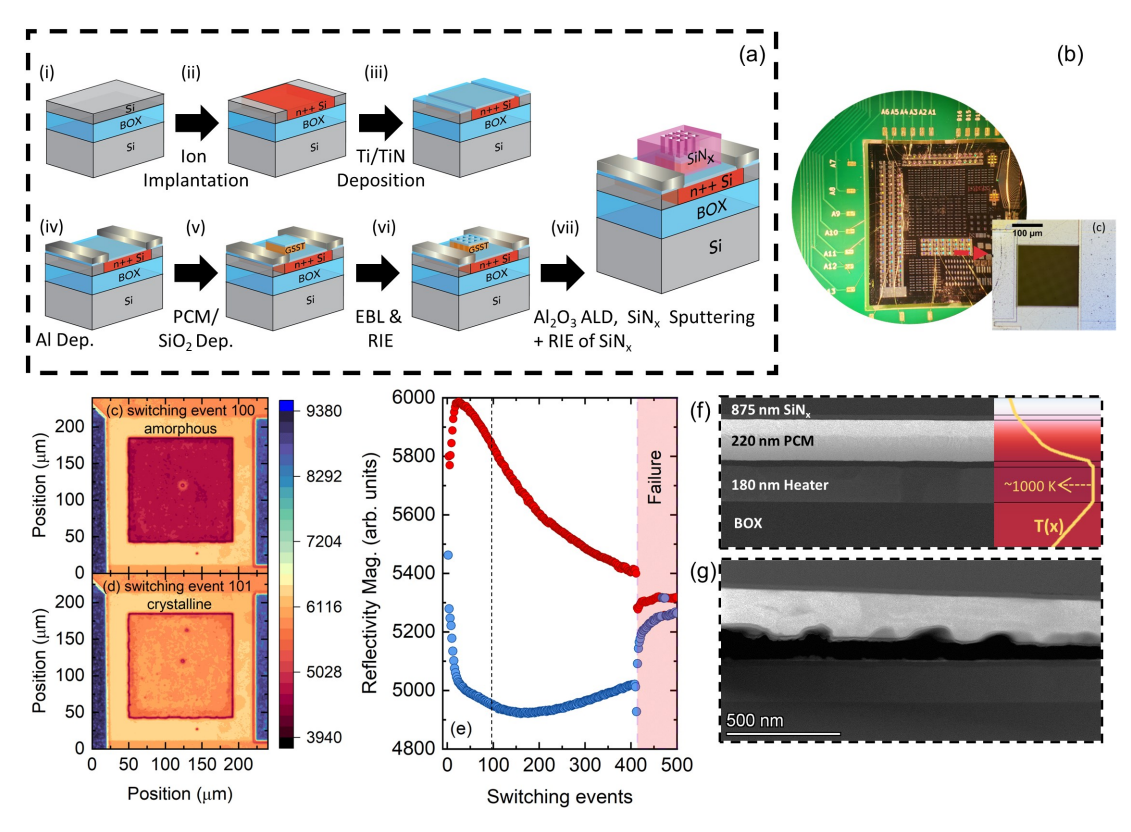


**Figure 2.** (a) Fabrication flow chart of the metasurface device. After encapsulation with silicon nitride and etch-back, aluminum metal apertures are deposited, and the sample is back-side polished via mechanical lapping to remove diffuse reflections. Afterwards, the sample is wire bonded to a printed circuit board. (b) Optical image of the chip after wirebonding. Different devices were fabricated with different periods, resulting in the various reflected colors. (c) Visible range optical micrograph of a fabricated metasurface device. The fringes observed in the images are Moiré artifacts from the specific magnification used, the camera pixel pitch and periodicity of the metasurface. (c,d) NIR image of an unpatterned PCM thin film test structure for degradation mechanism analysis, captured with front-side illumination during the switching events (c) 100 corresponding to amorphous state and (d) 101 corresponding to crystalline state. (e) The magnitude of reflected light from the surface of the PCM upon cycling detected by the IR camera. (f & g) TEM micrographs of the device and its associated layers before and after cycling.

### 2.3 Characterization Methods

The optical response of our PCM-based filter was evaluated using a FTIR spectrometer with an external Mercury Cadmium Telluride (MCT) detector. The beam was focused onto the backside of the sample with a spot size of 250  $\mu$ m in diameter using a reflective objective. After transmitting through the front of the sample, the beam was collected with another objective directed towards the detector. Since the focused beam is larger than the PCM metasurface, we deposited a 200  $\mu$ m  $\times$  200  $\mu$ m metallic aperture to restrict the beam so it only passes through the metasurface area. The transmission spectrum through a 200  $\mu$ m  $\times$  200  $\mu$ m square aperture (Thorlabs, Inc.), the same size as our metafilter, was also measured on the same setup to normalize the measured metasurface transmittance. In addition to the micro-FTIR measurement, a short-wave infrared (SWIR) camera (FLIR A6262) equipped with a long pass filter was used for detecting light within the range of 800 nm to 1700 nm. FTIR measurements allow us to capture the spectral transmission of the device, while the SWIR camera assists us in observing the devices' broadband response upon phase transformation.

# 3 Results and Discussion

In order to evaluate the performance of our PCM-based device upon switching between amorphous and crystalline states, we start our experiment by depositing a continuous patch of thin film GSST on top of the micro-heater prior to metasurface fabrication. The purpose of the test structure is to examine the contributing degradation mechanisms limiting endurance of PCM devices and inform mitigation strategies for our final metasurface device. The PCM film test structure has a slightly smaller coverage area (140 µm × 140 µm) than our subsequent metasurface device. The corresponding sheet resistance of the micro-heater is measured to be 42  $\Omega/\Box$ . For switching between the two states we used a 10  $\mu$ s, 45V pulse for amorphization (resulting in 0.48 mJ and  $1.4 \times 10^{10}$  J/m<sup>3</sup> across the heater, GSST and protective layer), and to switch back to crystalline state, a series of 200 ms priming pulses are sent to initiate nucleation area in the PCM and facilitate the phase transformation<sup>43, 44</sup>. These priming pulses incrementally increase from 10 to 16 V and are applied to the sample before the crystallization pulse. Subsequently, after 1 sec from the priming pulses a 18 V crystallization pulse lasting for 1 second is applied (resulting in a SET energy of 7.7 J and  $2.3 \times 10^{14}$  J/m<sup>3</sup>). There are 30 sec pauses between amorphization and crystallization to ensure complete thermal relaxation and that the device does not undergo electromigration. We observe slight differences in required switching voltage between devices, independent of whether they are thin-film or metasurface PCM. This is likely due to variations in microheater resistance and differences in wire bonding rather than changes in the structure of the PCM. For consistency, all experiments used a constant pulse width. However, the voltage needed for crystallization and amorphization differed between devices, ranging from 17-20 V for crystallization and 45-50 V for amorphization.

Figures 2(a,b) depict images captured by a SWIR camera upon transitioning from one phase to another, specifically at switching events of 100 and 101, corresponding to the amorphous and crystalline states, respectively. For better clarity, in this manuscript a "switching event" refers to a single phase transformation, while a "cycle" pertains to the process of transitioning to a different phase and subsequently returning to the original phase. Figure 2(c) shows the changes in surface reflectivity of the PCM upon cycling using the SWIR camera. As anticipated, the amorphous phase of GSST exhibits higher transparency in the near-infrared spectrum compared to the crystalline phase. Consequently, the reflection from the PCM-covered area is less pronounced in the amorphous phase compared to the crystalline phase. As can be seen in Fig. 2(c), at the initial stages of the cycling, the device shows changes in the reflectivity. As cycling continues, the switching contrast gradually enhances after several tens of cycles. Based on our examination through EDS microscopy line-scans (refer to Supplementary Note 3 and Figure S5 and S6), we attribute the burn-in behavior of the device<sup>45</sup> to the presence of Ge-rich regions in close proximity to the heater, and Sb and Te rich regions away from the heater, which are a consequence of the thermal evaporation deposition process. The Ge-rich area is expected to have a higher crystallization and melting temperature, which in turn gives rise to non-uniform switching temperatures throughout the thickness of the GSST laver<sup>46-48</sup>. With repeated cycling, we observe the migration of Ge away from the heater. This can be inferred also from the decrease in contrast in the dark-field TEM images between Fig. 2 (f) and (g), corresponding to a more uniform elemental distribution in comparison to the as deposited structure. As hundreds of cycles are completed, we begin to see small areas within the PCM-covered region stay unchanged upon switching. These areas gradually expand, leading to the gradual decrease in reflectance contrast from 20 to 400 switching events. A comprehensive set of images documenting the switching process from start to finish has been compiled into a video. This video is available in Supplementary Movie 1 and offers visual insight into the formation of damage on the micro-heater surface during the switching period.

We evaluate the failure mechanism by performing transmission electron microscopy (TEM) before and after 375 cycles (750 switching events) as well as using computational models to estimate the temperature distribution in the device. Figure 2(d) presents the layer configuration in the device and the model used in our simulations, along with the corresponding temperature increase at the heater. Our observations reveal that during cycling, the temperature peaks at the electrode/PCM interface and reaches as high as 1000 K the during amorphization cycle, giving rise to maximum thermal stress at the interface. Interestingly, our TEM result after failure, given in Fig. 2(e), indicates that the device undergoes delamination from this very interface.

Multiple factors could contribute to the delamination of the PCM, such as volume contraction of GSST upon crystallization (approximately  $3-5\%^{49,50}$ ), disparate thermal expansion coefficients between the layers, inadequate adhesion between the PCM and the electrode, and insufficient thermo-mechanical durability of the encapsulating  $SiN_x$  layer. Our prior research has demonstrated that a  $SiN_x$  layer with inferior mechanical properties can significantly impair the device's lifetime<sup>51</sup>.

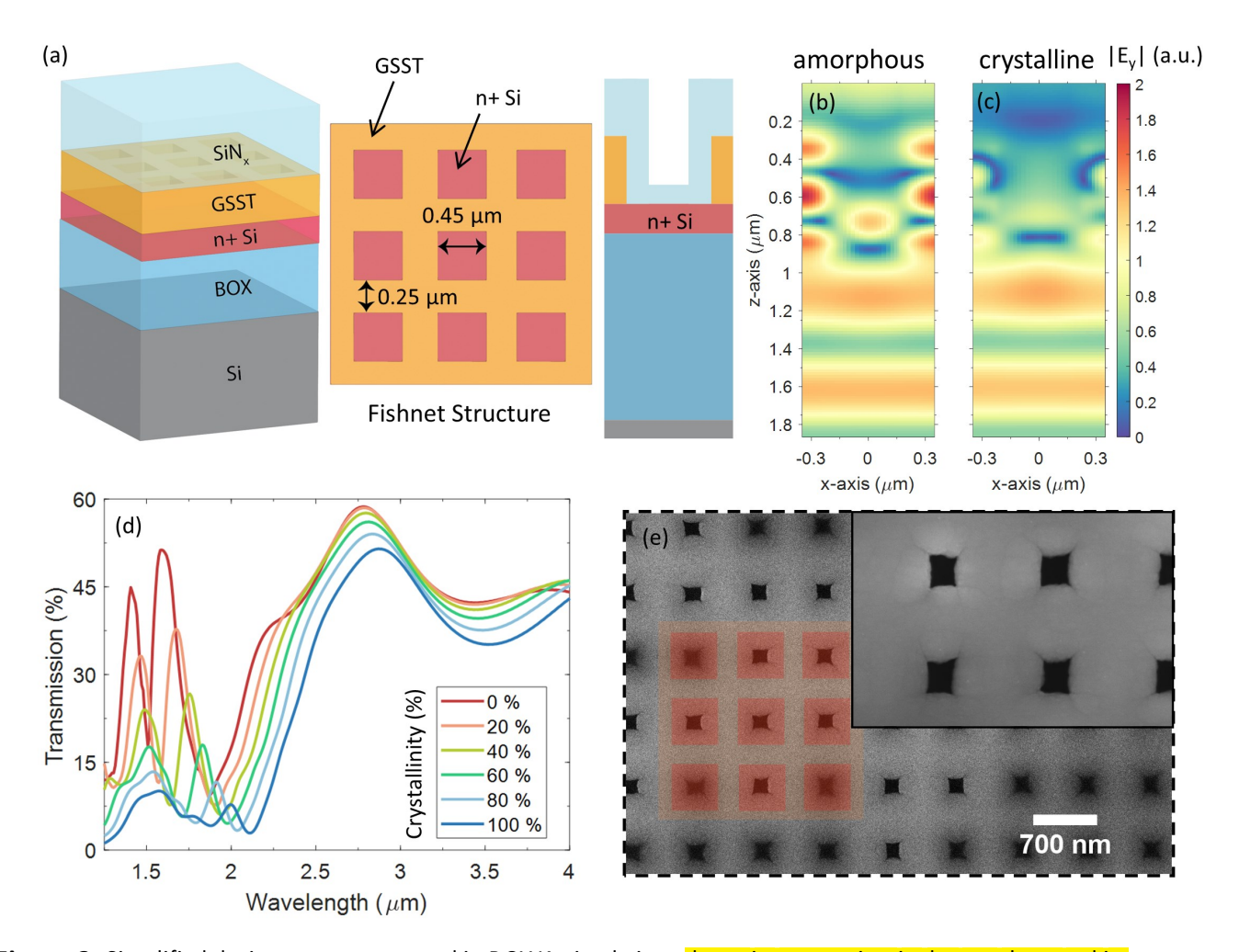


**Figure 3.** Simplified device structure assumed in RCWA simulations shown in perspective, in the x-y plane, and in cross-section (a) along with  $|E_y|$  in the meta-atom in the fully amorphous (b) and crystalline (c) state at 1420 nm for normal incidence, polarization along  $\hat{Y}$ . Simulated transmission curves averaged over TE and TM and over angles up to 16°. An SEM image of the metafilter surface. The inset shows the air holes remaining after silicon nitride deposition along with the morphology changes at the edges, likely due to raised nitride due to a higher deposition rate at the GSST edges (e).

Evaluating the thin-film PCM on the microheater provided us with crucial insights into the switching behavior and failure mechanisms in this specific device architecture. This understanding, derived from the performance analysis of the heater with thin-film PCM, is vital in informing the design process for a more effective and durable filter. Since delamination constitutes the main degradation mechanism, we hypothesize that a fishnet metasurface structure as illustrated in Fig. 3 (a,e), can alleviate the mechanical failure and yield durable filter devices. First, the top capping layers (Al<sub>2</sub>O<sub>3</sub> + SiN<sub>x</sub>) that encapsulate the PCM can be in direct contact with the SiO<sub>2</sub> covered heater surface through holes in the fishnet structure. Given the excellent adhesion between SiO<sub>2</sub> and atomic layer deposited Al<sub>2</sub>O<sub>3</sub>, we expect that the contacts between them can act as anchor points to impede delamination of the PCM structures<sup>52,53</sup>. Second, the large surface areas of the fishnet structures can also effectively relieve the mechanical stress. Furthermore, compared to typical "pillar" metasurfaces, we found that the fishnet design improved switching consistency since crystallization can efficiently propagate across the entire structure through crystalline growth without necessitating nucleation in each individual meta-atom, which is highly stochastic in small structures exemplified by "pillar" meta-atoms.

Based on the fishnet geometry, we deployed RCWA simulations to engineer a PCM-based metasurface specifically for

filtering purposes. The simulated transmission spectra of the sample as a function of crystalline volume fraction are given in Fig. 3 (d). The main features are a significant decrease in transmission centered at 1.6  $\mu$ m wavelength with increased crystalline fraction, along with a red-shift of the spectral peaks observed due to an increase in the index of GSST. The transmission envelope overall shrinks due to increased absorption in the crystalline state. Simulations of the propagating electric field through the structure show higher field intensity in the PCM region and nitride cladding in the amorphous state for a wavelength with higher transmission (Fig. 3 b). The increased absorption and index of the crystalline structure leads to a weaker field amplitude in the PCM region, with most of the signal being reflected back (Fig. 3 c).

Following the fabrication of the PCM-based metasurface on the microheater, we proceeded to assess the device's transmission characteristics across a wavelength range spanning from 1.25 to 4  $\mu$ m using FTIR spectroscopy. Given the device's compact dimensions, we developed an in-house micro-FTIR setup. In Fig. 4(a), one can observe a schematic of the experimental setup used for this purpose. As depicted in Fig. 4(a), the output from the FTIR spectrometer, which is approximately 2 inches in diameter, passes through a beam condenser comprising a pair of CaF<sub>2</sub> lenses for resizing it to fit the aperture of the focusing objective, which focuses the beam to match the metasurface size. After the beam passes through the device, the light is recollected with a secondary objective and directed towards an external Mercury Cadmium Telluride (MCT) detector. A flip mirror is inserted on the path of the beam to align the beam to the specific device under test. For a more detailed explanation of the measurement procedure, including signal strength and background collection, refer to Supplementary Note 1.

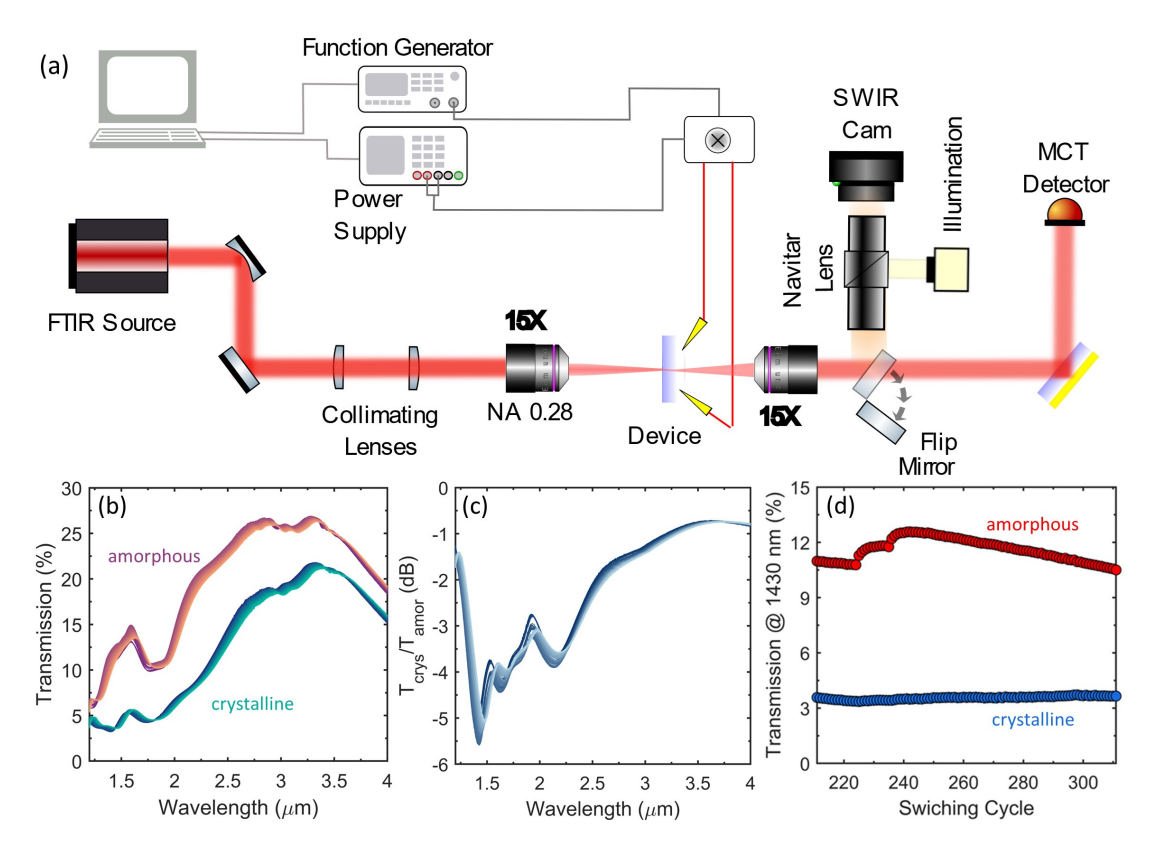


**Figure 4.** (a) Schematic of the measurement setup for the FTIR spectral data collection. (b) Transmission spectra upon switching between amorphous and crystalline states over the course of 100 cycles. (c) Transmission ratio between amorphous and crystalline phases as a function of wavelength. The inset shows the drift of the maximum contrast to larger wavelengths over the 100 cycles. (d) Transmission magnitude for amorphous and crystalline state at 1430 nm. The jump points were triggered by slight adjustments to the amorphization voltage.

The experimental results presented in Fig. 4(b) show trends similar to those predicted in simulations, in particular suppression of the transmission peak at  $1.6~\mu m$  wavelength as well as the overall transmission reduction at wavelengths above  $2.0~\mu m$  during the transition from the amorphous to the crystalline state. Peak transmission contrast exceeding 5.5~dB was obtained near the  $1.43~\mu m$  wavelength (Fig. 4 d). To validate switching consistency, the measured spectra over 100~s witching cycles were overlaid in Fig. 4 (c) and (d). To provide further insight into these results, the absolute transmittance at 1430~nm as a function of cycle number for both amorphous and crystalline states are plotted in Fig. 4 (d). The switching behavior was observed to be relatively stable throughout the 100~c cycles. The kinks at cycles 225~and~236~for the amorphous state were due

to adjustments to the amorphization voltage as part of the switching parameter optimization process. We hypothesize that the difference between the measured transmission and the simulated transmission may be attributed, in part, to imperfections arising during the fabrication process. These imperfections could include surface roughness resulting from processes like RIE or sputtering, as well as additional scattering at grain boundaries. Furthermore, deviations in input optical constants used in the simulation from the actual deposited values, as well as the possibility of trace crystallites post-amorphization, may contribute to this discrepancy.

To further evaluate the performance of the fabricated filters and gain insights into the switching characteristics across the heater's surface, we employed a SWIR camera to image the entire surface of the PCM-based metasurface upon switching. For this, similar to FTIR measurements as depicted in Fig. 5(a), we directed the broadband IR beam onto the  $200\mu m \times 200\mu m$  device, and used the camera as the detector. After each switching event, the SWIR camera captures an image of the device surface and monitors any potential damage during cycling. In this arrangement, the sample is backlit by a focused IR beam, while the camera, positioned in front, records the transmitted light intensity. Figure 5(b) displays a real-time image of the sample being tested, highlighting the focused beam as it passes through the PCM-based tunable filter. A complete video detailing the switching cycles of this filter from start to finish can be found in Supplementary Movie 2.

A further demonstration of the metafilter's capabilities is depicted in panels Fig. 5(f-h). In this setup, a glass slide with an etched metal mask featuring the NASA worm logo was positioned in the beam path immediately after the light source. This mask selectively allows light to pass only through the etched NASA logo as illustrated in Fig. 5(a). Through this arrangement, we can turn the NASA logo on and off by changing the phase of the PCM in the metasurface using electrical pulses. As seen in panel Fig. 5(f), in the amorphous state, the filter is in high transmission mode and thus, the NASA logo is clearly visible at the camera, whereas in the crystalline state when the filter is in blocking mode, the intensity of the logo is significantly suppressed. Similarly, as depicted in Fig. 5(h), applying an amorphization pulse, can effectively restore the NASA logo. This process can be done reversibly leveraging just electrical stimuli. A video featuring the images from each cycle is available in Supplementary Movie 3 for further reference.

It is important to highlight that while our focus in this work was on optimizing the metasurface structure for amplitude contrast, it is entirely feasible to also optimize it for phase contrast as well. To achieve efficient phase modulation, both the extinction coefficient of the PCM and the doped silicon should be sufficiently low to enable large quality factor resonances. This would allow us to identify meta-atoms within the parameter space that exhibit comparable (preferably high) transmission while also displaying a significant range in phase shift between their amorphous and crystalline states. This consideration assumes that the phase delay is not primarily derived from treating the meta-atoms as long waveguides perpendicular to the substrate. To achieve high Q resonances, a lower loss PCM is almost mandatory and it is possible even larger modulation volume. This hints at a problem that the research community will need to solve. For on-demand, non-volatile PCM metasurfaces with more complex transfer functions like beam steerers, holograms, lenses, etc., we will need to use lower loss materials that still allow for sufficiently large modulation volume so that 2π phase shift can be achieved at a given wavelength just by changing the phase of the material.

In this study, we designed, fabricated, and demonstrated the performance of an all solid-state, non-volatile reconfigurable metafilter without the use of any mechanical moving parts. Our work takes advantage of a PCM-based metasurface that is capable of switching between a high- and low-transmittance state by applying electrical pulses within a microelectronic circuitry framework. We have also identified delamination as the leading failure mechanism in the device and implemented a fishnet metasurface design to enhance its endurance to 1250 cycles, which represents a 25-fold improvement over previously reported PCM-based metasurfaces of comparable aperture size. The fishnet structure provides an interconnected network that facilitates growth of crystals uniformly through the structure and therefore it can prove advantageous for low loss PCM (such as GSST, Sb<sub>2</sub>Se<sub>3</sub> and Sb<sub>2</sub>S<sub>3</sub>) where growth plays a more significant role in the crystallization process. This work introduces a reliable platform for switching PCM-based metasurfaces, opening up new possibilities in low-power reconfigurable optics and programmable photonics across various applications.

# 4 Disclaimer

Specific vendor and manufacturer names are explicitly mentioned only to accurately describe the test hardware. The use of vendor and manufacturer names does not imply an endorsement by the U.S. Government nor does it imply that the specified equipment is the best available.

#### References

- 1. Horst, Y. et al. Tbit/s line-rate satellite feeder links enabled by coherent modulation and full-adaptive optics. Light. Sci. & Appl. 12, 153 (2023).
- 2. Hampson, K. M. et al. Adaptive optics for high-resolution imaging. Nat. Rev. Methods Primers 1, 68 (2021).

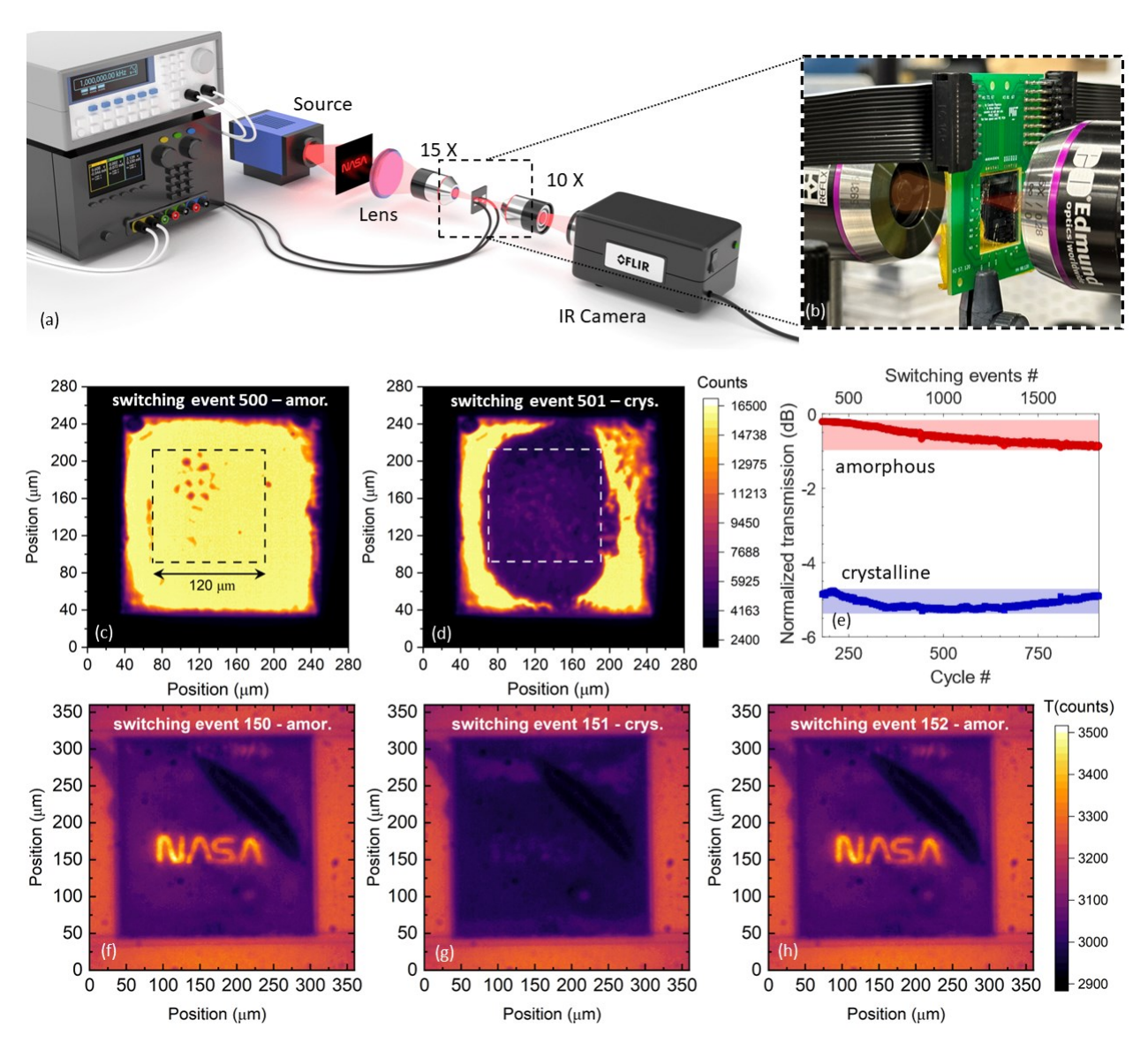


**Figure 5.** (a) An illustration of the measurement arrangement, featuring a focused beam passing through the metafilter. (b) A real-time image of the sample being tested. The infrared camera image captured when the broadband beam is passing through the device in its (c) amorphous and (d) crystalline phase. (e) The mean count value across 14000 pixels within the square marked by dashed lines, over 700 stable cycles. The full testing data is available in Supplementary Note 1 Fig. S3 (b). Panels (f-h) illustrate the imaging performance of a PCM-based metafilter in its activated (on) and deactivated (off) states. The dark streak over NASA worm logo is a delaminated region.

- 3. Davies, R. & Kasper, M. Adaptive optics for astronomy. Annu. Rev. Astron. Astrophys. 50, 305-351 (2012).
- 4. Salter, P. S. & Booth, M. J. Adaptive optics in laser processing. Light. Sci. & Appl. 8, 110 (2019).
- 5. Algorri, J. F., Zografopoulos, D. C., Urruchi, V. & Sánchez-Pena, J. M. Recent advances in adaptive liquid crystal lenses. Crystals 9, 272 (2019).
- 6. Madec, P.-Y. Overview of deformable mirror technologies for adaptive optics and astronomy. In Adaptive Optics Systems III, vol. 8447, 22–39 (SPIE, 2012).
- 7. Beichman, C. A. et al. Science opportunities with the near-ir camera (NIRCam) on the james webb space telescope (JWST). In Space Telescopes and Instrumentation 2012: Optical, Infrared, and Millimeter Wave, vol. 8442, 973–983 (SPIE, 2012).
- 8. Ren, Y.-X., Lu, R.-D. & Gong, L. Tailoring light with a digital micromirror device. Annalen der physik 527, 447–470 (2015).

- 9. Gyger, S. et al. Reconfigurable photonics with on-chip single-photon detectors. Nat. communications 12, 1408 (2021).
- 10. Gu, T., Kim, H. J., Rivero-Baleine, C. & Hu, J. Reconfigurable metasurfaces towards commercial success. Nat. Photonics 17, 48–58 (2023).
- 11. Zhang, Y. et al. Electrically reconfigurable non-volatile metasurface using low-loss optical phase-change material. Nat. Nanotechnol. 16, 661–666 (2021).
- 12. Abdollahramezani, S. et al. Electrically driven reprogrammable phase-change metasurface reaching 80% efficiency. Nat. communications 13, 1696 (2022).
- 13. Wu, P. C. et al. Dynamic beam steering with all-dielectric electro-optic III–V multiple-quantum-well metasurfaces. Nat. Commun. 10, 3654, DOI: 10.1038/s41467-019-11598-8 (2019).
- 14. Iyer, P. P., Decrescent, R. A., Lewi, T., Antonellis, N. & Schuller, J. A. Uniform Thermo-Optic Tunability of Dielectric Metalenses. Phys. Rev. Appl. 10, 044029, DOI: 10.1103/PhysRevApplied.10.044029 (2018).
- 15. Kim, Y. et al. Phase Modulation with Electrically Tunable Vanadium Dioxide Phase-Change Metasurfaces. Nano Lett. 19, 3961–3968, DOI: 10.1021/acs.nanolett.9b01246 (2019).
- 16. Yin, X. et al. Beam switching and bifocal zoom lensing using active plasmonic metasurfaces. Light. Sci. & Appl. 6, e17016, DOI: 10.1038/lsa.2017.16 (2017).
- 17. Julian, M. N., Williams, C., Borg, S., Bartram, S. & Kim, H. J. Reversible optical tuning of GeSbTe phase-change metasurface spectral filters for mid-wave infrared imaging. Optica 7, 746–754 (2020).
- 18. Raeis-Hosseini, N. & Rho, J. Metasurfaces based on phase-change material as a reconfigurable platform for multifunctional devices. Materials 10, 1046 (2017).
- 19. de Galarreta, C. R. et al. Reconfigurable multilevel control of hybrid all-dielectric phase-change metasurfaces. Optica 7, 476–484 (2020).
- 20. Wang, M. et al. Varifocal metalens using tunable and ultralow-loss dielectrics. Adv. Sci. 10, 2204899 (2023).
- 21. Shaltout, A. M., Shalaev, V. M. & Brongersma, M. L. Spatiotemporal light control with active metasurfaces. Science 364, eaat3100 (2019).
- 22. Cao, T. & Cen, M. Fundamentals and applications of chalcogenide phase-change material photonics. Adv. Theory Simulations 2, 1900094, DOI: https://doi.org/10.1002/adts.201900094 (2019). https://onlinelibrary.wiley.com/doi/pdf/10. 1002/adts.201900094.
- 23. Wuttig, M., Bhaskaran, H. & Taubner, T. Phase-change materials for non-volatile photonic applications. Nat. photonics 11, 465–476 (2017).
- 24. Wright, C. D., Bhaskaran, H. & Pernice, W. H. Integrated phase-change photonic devices and systems. MRS Bull. 44, 721–727 (2019).
- 25. Ding, F., Yang, Y. & Bozhevolnyi, S. I. Dynamic metasurfaces using phase-change chalcogenides. Adv. Opt. Mater. 7, 1801709, DOI: https://doi.org/10.1002/adom.201801709 (2019). https://onlinelibrary.wiley.com/doi/pdf/10.1002/adom. 201801709.
- 26. Aryana, K. et al. Optical and thermal properties of ge 2 sb 2 te 5, sb 2 se 3, and sb 2 s 3 for reconfigurable photonic devices. Opt. Mater. Express 13, 3277–3286 (2023).
- 27. Zhang, Y. et al. Myths and truths about optical phase change materials: A perspective. Appl. Phys. Lett. 118 (2021).
- 28. Zhang, H. et al. Miniature multilevel optical memristive switch using phase change material. ACS Photonics 6, 2205–2212 (2019).
- 29. Zhang, H. et al. Nonvolatile waveguide transmission tuning with electrically-driven ultra-small GST phase-change material. Sci. Bull. 64, 782–789 (2019).
- 30. Wei, M. et al. " zero change" platform for monolithic back-end-of-line integration of phase change materials in silicon photonics. arXiv preprint arXiv:2308.15723 (2023).
- 31. Zheng, J. et al. Nonvolatile electrically reconfigurable integrated photonic switch enabled by a silicon PIN diode heater. Adv. Mater. 32, 2001218 (2020).
- 32. Erickson, J. R. et al. Comparing the thermal performance and endurance of resistive and PIN silicon microheaters for phase-change photonic applications. Opt. Mater. Express 13, 1677–1688 (2023).

- 33. Fang, Z., Chen, R., Zheng, J. & Majumdar, A. Non-volatile reconfigurable silicon photonics based on phase-change materials. IEEE J. Sel. Top. Quantum Electron. 28, 1–17, DOI: 10.1109/JSTQE.2021.3120713 (2022).
- 34. Ríos, C. et al. Ultra-compact nonvolatile phase shifter based on electrically reprogrammable transparent phase change materials. PhotoniX 3, 26 (2022).
- 35. Fang, Z. et al. Non-volatile phase-only transmissive spatial light modulators. arXiv preprint arXiv:2307.12103 (2023).
- 36. Kim, H. J. et al. Versatile spaceborne photonics with chalcogenide phase-change materials. npj Microgravity 10, 20 (2024).
- 37. Hugonin, J. P. & Lalanne, P. RETICOLO software for grating analysis (2021).
- 38. Markel, V. A. Introduction to the Maxwell Garnett approximation: tutorial. J. Opt. Soc. Am. A 33, DOI: 10.1364/josaa.33. 001244 (2016).
- 39. Zhang, Y. et al. Broadband transparent optical phase change materials for high-performance nonvolatile photonics. Nat. Commun. 10, 4279, DOI: 10.1038/s41467-019-12196-4 (2019).
- 40. Popescu, C.-C. et al. An open-source multifunctional testing platform for optical phase change materials. Small Sci. n/a, 2300098, DOI: https://doi.org/10.1002/smsc.202300098 (2023). https://onlinelibrary.wiley.com/doi/pdf/10.1002/smsc.202300098.
- 41. Romero-García, S., Merget, F., Zhong, F., Finkelstein, H. & Witzens, J. Silicon nitride cmos-compatible platform for integrated photonics applications at visible wavelengths. Opt. express 21, 14036–14046 (2013).
- 42. Zimmer, G. & Vogt, H. Cmos on buried nitride—a vlsi soi technology. IEEE transactions on electron devices 30, 1515–1520 (1983).
- 43. Orava, J. & Greer, A. L. Classical-nucleation-theory analysis of priming in chalcogenide phase-change memory. Acta Materialia 139, 226–235, DOI: 10.1016/j.actamat.2017.08.013 (2017).
- 44. Aryana, K. et al. Toward accurate thermal modeling of phase change material based photonic devices. Small (2023).
- 45. Xiong, F. et al. Self-aligned nanotube—nanowire phase change memory. Nano Lett. 13, 464–469, DOI: 10.1021/nl3038097 (2013). PMID: 23259592, https://doi.org/10.1021/nl3038097.
- 46. Redaelli, A., Petroni, E. & Annunziata, R. Material and process engineering challenges in Ge-rich gst for embedded pcm. Mater. Sci. Semicond. Process. 137, 106184 (2022).
- 47. Cecchi, S. et al. Crystallization and electrical properties of Ge-rich GeSbTe alloys. Nanomaterials 12, 631 (2022).
- 48. Zuliani, P. et al. Overcoming temperature limitations in phase change memories with optimized Ge<sub>x</sub>Sb<sub>y</sub>Te<sub>z</sub>. IEEE Transactions on Electron Devices 60, 4020–4026, DOI: 10.1109/TED.2013.2285403 (2013).
- 49. Shalaginov, M. Y. et al. Reconfigurable all-dielectric metalens with diffraction-limited performance. Nat. communications 12, 1225 (2021).
- 50. Aryana, K. et al. Suppressed electronic contribution in thermal conductivity of Ge2Sb2Se4Te. Nat. Commun. 12, 1–9, DOI: 10.1038/s41467-021-27121-x (2021).
- 51. Popescu, C.-C. et al. Long live O-PCMs: Understanding reliability challenges of optical phase change materials. In CLEO: Science and Innovations, STh1O–5 (Optica Publishing Group, 2023).
- 52. Ding, J. et al. The influence of substrate on the adhesion behaviors of atomic layer deposited aluminum oxide films. Surf. Coatings Technol. 205, 2846–2851 (2011).
- 53. Takakura, R., Murakami, S., Watanabe, K. & Takigawa, R. Room-temperature bonding of Al<sub>2</sub>O<sub>3</sub> thin films deposited using atomic layer deposition. Sci. reports 13, 3581 (2023).

# Data availability.

The data that support the findings of this study are available from the corresponding author upon reasonable request.

# Acknowledgements

The lead authors extend their gratitude to Mr. Scott M. Bartram for his valuable insights and discussions concerning the experimental setup. Special thanks are extended to Mr. Ronald Neale and Mr. Stanley H. Husch for their contributions to graphic design. This work was carried out in part through the use of MIT.nano's facilities. This work was partially supported by the Air Force Office of Scientific Research (AFOSR), award numbers FA9550-22-1-0456 and FA9550-22-1-0532. This research

was sponsored by the National Aeronautics and Space Administration (NASA) through a contract with ORAU. The views and conclusions contained in this document are those of the authors and should not be interpreted as representing the official policies, either expressed or implied, of the National Aeronautics and Space Administration (NASA) or the U.S. Government. The U.S. Government is authorized to reproduce and distribute reprints for Government purposes notwithstanding any copyright notation herein.

# **Author contributions**

K.A., C.C.P., H.J.K., and J.H. designed the study. C.C.P. performed the photonic device design and fabricated the metasurface samples. H.J.K. and P.G. fabricated the logos. K.A., P.G., and C.C.P. performed the characterization. K.A. and K.P.D. performed the COMSOL simulations. S.V. and V.L. fabricated the SOI micro-heater platform. H.B.B. and T.W.L. performed STEM sample preparation and imaging. C.A.R.O., Y.Z. and M.J. designed the SOI micro-heater platform. K.A., C.C.P. and J.H. wrote the manuscript. M.K. and K.A.R. provided the bulk phase change materials. All authors contributed to technical discussions and revising the manuscript.

# **Competing interests**

The authors declare no competing interests.

Correspondence and requests for materials should be addressed to K.A. or H.J.K.